KeAi
CHINESE ROOTS
GLOBAL IMPACT

Available online at www.keaipublishing.com/en/journals/journal-of-magnesium-and-alloys/

ScienceDirect

Journal of Magnesium and Alloys 13 (2025) 3829–3846

www.elsevier.com/locate/jma

Full Length Article

# Additive manufacturing high-strength and ultra-high-rare-earth magnesium alloys: Excellent long-time aging hardening and strengthening behavior ☆

Zhe Xu [a], Zhuo Li [a,b,*], Chunjie Shen [a], Dongdong Zheng [a], Yuxuan Tu [b]

[a] National Engineering Laboratory of Additive Manufacturing for Large Metallic Components, School of materials science & engineering, Beihang University, Beijing, 100191, China

[b] Ningbo Institute of Technology, Beihang University, Ningbo, 315800, China

Received 10 February 2025; received in revised form 15 March 2025; accepted 12 April 2025
Available online 10 May 2025

**Abstract**

Gadolinium (Gd) is one of the most effective strengthening elements for magnesium alloys. The development of commercially available Mg-Gd alloys with high Gd content and the optimization of their preparation processes have been a major focus in magnesium alloy research. In this study, a Mg-23Gd-2Zn-0.4Zr alloy with ultra-high Gd content is designed, and high-quality fabrication is achieved using laser-directed energy deposition (LDED) technology. Through heat treatment and microstructure control, a balance between tensile strength (425 MPa) and elongation (3.4%) is achieved. The ultra-high strength of the LDED-T6 VZ232K alloy is primarily attributed to precipitation strengthening caused by the ultra-high density ($2.4 \times 10^4$ $\mu m^{-2}$) of $\beta'$ phase. The high ductility is mainly due to the modification of the fracture mode, facilitated by the introduction of a substantial number of stacking fault structures during solution heat treatment. The extended hardness plateau (exceeding 138 Hv) and high yield strength (exceeding 300 MPa) are associated with the three-directional cross-interlocked structure of the $\beta'$ phase in the over-aged state at 220 °C and 250 °C. The analysis of the LDED-VZ232K alloy indicates that reduced heat input during the additive manufacturing (AM) process is critical for the defect-free fabrication of alloys with ultra-high Gd content.


*Keywords:* LDED; Mg-Gd-Zn-Zr; Heat treatment; Precipitates evolution.

## 1. Introduction

The density of magnesium is only two-thirds that of aluminum alloys, and it exhibits excellent specific stiffness and specific strength. Currently, the demand for lightweight materials in the aerospace industry is increasing [1]. However, the absolute strength of materials remains the primary criterion for their application. The relatively low absolute strength of magnesium alloys significantly limits their use in aerospace components, restricting their application to non-load-bearing or secondary parts, such as aircraft propeller housings, chassis, and transfer boxes [2]. Among magnesium alloys, the Mg-Gd series alloy exhibits the highest absolute strength [3], making it a focal point of research and industrial interest.

Gadolinium (Gd) exhibits a high degree of solid solubility in magnesium, and Gd processes the greatest tendency to decrease in solid solubility with decreasing temperature compared to other rare earth elements in Mg [4]. Consequently, Mg-Gd alloys display the optimal solid solution strengthening and precipitation strengthening subsequent to heat treatment [5]. The most significant precipitation strengthening phases in Mg-Gd alloys during the aging process are nanoscale metastable $\beta$ series phases [6], particularly the $\beta'$ phase ($Mg_7RE$, orthorhombic). The $\beta'$ phase impedes the movement of basal dislocations, thereby enhancing the mechanical properties of the alloys [7]. Recent studies have demonstrated that an augmentation in Gd content gives rise to a higher number density and aspect ratio of the $\beta'$ phase [8], thereby enhancing the strength of the alloy. For instance, the yield

☆ Peer review under the responsibility of Chongqing University.

* Corresponding author.
*E-mail address:* lizhuo@buaa.edu.cn (Z. Li).

https://doi.org/10.1016/j.jma.2025.04.007

strength of Mg-15Gd-3Y-0.2Zr is elevated from 170 MPa to 230 MPa compared with Mg-9Gd-3Y-0.2Zr, and the yield strength is augmented by approximately 10 MPa for every 1 wt.% increase in Gd content [9]. The yield strength of the cast GW103K alloy after heat treatment has been determined to be 245 MPa, while that of the cast GW63K alloy is 188 MPa [10]. It is obvious that the enhancement of Gd content serves to enhance the age-strengthening effect. Despite the significant efforts of numerous researchers to enhance the strength of Mg-Gd alloys through the augmentation of Gd content, it has proven challenging to surpass the upper limit (approximately 20 wt.% ) [11], of the Mg-Gd alloys that can be effectively prepared. Identifying a viable preparation method to increase Gd content beyond this limit is expected to break through these compositional constraints. Such a method will enable the coexistence of multiple strengthening mechanisms, ultimately producing Mg-Gd alloys with exceptional absolute strength.

The plasticity of Mg-Gd alloys decreases significantly with increasing Gd content, and the issue of room-temperature brittleness remains unavoidable [12]. Consequently, balancing the relationship between strength and plasticity while increasing Gd content has been a persistent focus of research. Traditional casting processes aim to activate non-basal slip systems by incorporating elements such as Zn to control the formation of long-period stacking ordered (LPSO) phases, $\gamma$ phases, and $\beta$-series phases in Mg-Gd alloys [13], thereby achieving improvements in both strength and plasticity. However, due to the presence of coarse dendrites and inhomogeneous elemental distribution in cast Mg alloys, increasing Gd content exacerbates segregation at grain boundaries, significantly degrading mechanical properties [14]. In contrast to cast magnesium alloys, wrought magnesium alloys demonstrate a notable enhancement in key strengthening mechanisms. The deformation process increases dislocation density and refines recrystallized grains through the introduction of severe plastic deformation [15], resulting in significantly higher strength compared to cast magnesium alloys [16]. Nevertheless, the inherent low plasticity of high-Gd magnesium alloys makes them prone to cracking during plastic processing [17], rendering effective deformation challenging to achieve. Therefore, developing an effective method for preparing magnesium alloys with high Gd content is critically important.

Compared to traditional manufacturing methods such as casting and deformation, additive manufacturing (AM) technology is characterized by rapid solidification in a small molten pool. During the solidification process, the liquid-solid interface moves faster than the diffusion rate of solute atoms in the liquid phase, resulting in a “solute trapping” effect [18]. This phenomenon enables the dissolution of excess solute atoms into the solid phase, thereby mitigating the issue of grain boundary segregation in the production of alloys with high rare earth element (REE) content. This dissolution process facilitates the production of magnesium alloys with high Gd content, uniform composition, and fine grain size [19]. Consequently, for the same composition, particularly those with high REE content, additive manufacturing technology demonstrates superior mechanical properties compared to traditional cast alloys.

For example, Deng et al. fabricated GWZ1221M [20] and GZ151K [17] alloys using laser powder bed fusion (LPBF) technology, achieving deposited grain sizes of 4.3 μm and 2.87 μm, respectively. The yield strengths of these alloys after solution aging and direct aging heat treatments reached 320 MPa and 405 MPa, demonstrating excellent mechanical properties. Similarly, Zhan et al. produced GW93K [21] alloy via wire arc additive manufacturing (WAAM) technology, achieving a strong combination of tensile strength (392 MPa) and elongation (3.3%) after heat treatment. The primary strengthening mechanisms in these alloys were fine grain strengthening and precipitation strengthening. However, as the rare earth element (REE) content increases, the cold crack sensitivity of parts fabricated by LPBF technology also rises due to its ultra-high cooling rates and temperature gradients [17], making it challenging to produce defect-free components. Additionally, the wires required for WAAM technology are typically derived from magnesium alloy ingots through a drawing process. However, the poor workability of high-Gd magnesium alloy ingots makes it difficult to obtain usable wires. In contrast, the powder used in laser-directed energy deposition (LDED) technology, which can accommodate higher rare earth content, is more readily available. Moreover, by controlling the cooling rate and temperature gradient during solidification, the formation of cold cracks can be effectively mitigated. For instance, Jiang [9], Zheng [22], and others have successfully produced defect-free LDED-GW183K and LDED-GA151K alloys. Therefore, LDED technology is the most promising approach for the successful production of ultra-high rare earth magnesium alloys.

In this study, a Mg-23Gd-2Zn-0.4Zr alloy with maximum Gd solid solubility in Mg is designed, and fully dense specimens free of visible defects are successfully fabricated using laser-directed energy deposition (LDED) technology. The effects of heat treatment on microstructure evolution and mechanical properties have been systematically investigated. The grain refinement mechanism of the as-deposited alloy is elucidated, with particular emphasis on the formation mechanisms of stacking faults (SFs) and long-period stacking ordered (LPSO) phases in T4-treated samples. Furthermore, the correlation between precipitate phase evolution and mechanical properties (yield strength and hardness) under peak-aged and over-aged conditions is quantitatively established. This work provides fundamental insights for advancing additive manufacturing of high-REE magnesium alloys.

## 2. Material and methods

### 2.1. Sample preparation and heat treatment

In our previous study [23], low REE powders could be deposited as high REE blocks by controlling the evaporation of Mg elements during the deposition process. However, the evaporation loss of a large amount of Mg element during the deposition process increases the defects of the deposited sam-

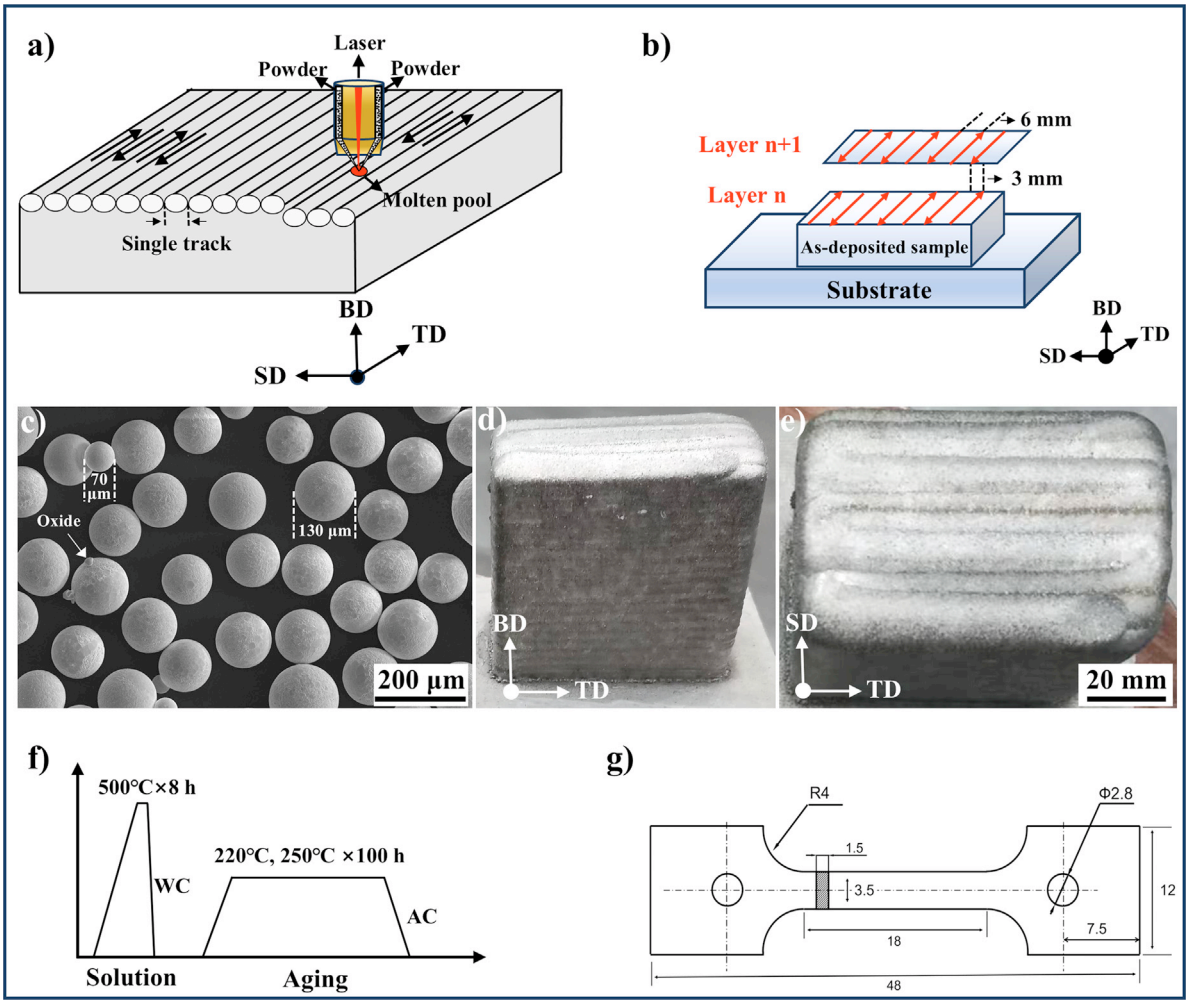


Fig. 1. (a) LDED deposition process; (b) LDED deposition path; (c) VZ232K powder morphology; (d, e) VZ232K as deposited block morphology; (f) heat treatment process regime; (g) plate tensile specimen dimensions.

ple and increases the risk of the deposition process. Therefore, building on previous work, the power of the LDED process in this experiment is reduced to 800 W and the scanning speed is increased to 1000 mm/min, effectively reducing the heat input of the deposition process. The scanning path of the deposition process is a bow-step scanning path along the TD direction (Fig. 1a), with an interval between the two scanning paths of 6 mm (Fig. 1b). As shown in Fig. 1c the powders used in this study exhibit a high degree of sphericity, with mean diameters ranging from 70–130 μm. A minimal amount of fine spherical oxides is produced during the inerting process to ensure the stability of the magnesium alloy powders. A complete block measuring 75 × 40 × 90 mm with no apparent defects or cracks is obtained after deposition (Fig. 1d and e), which demonstrat the feasibility of LDED technology for the preparation of large-size high REE magnesium alloys. The specimens are then placed in a muffle furnace for 500 × 8 h (T4) heat treatment, followed by water cooling treatment after reaching the designated time. Subsequently, the T4 state samples are transferred into a low-temperature aging furnace, where they are aged at 220 °C 100 h and 250 °C (T62) for 100 h, respectively. Following the completion of the aging process, the samples are air-cooled (Fig. 1f).

### 2.2. Microstructure characterization and property measurement

In this study, all specimens used for microstructure characterization analysis and mechanical property testing are obtained from the as deposited alloy in the BD orientation. Morphology and composition of the second phase are analyzed by using a Phenom G5 scanning electron microscope (SEM). The samples are mechanically ground and ion thinned to prepare a 3 mm diameter, 60 μm thickness sheet. The samples after electrolytic polishing are subjected to Electron Backscatter Diffraction (EBSD) testing, and the OIM 8 software is used for all subsequent data processing. The more microscopic morphology and crystal structure of the second phase are analysed by using a transmission electron microscope (FEI TECNAI G2 F30). The nanoindentation tests are conducted on the Nano Indenter G200X equipment. The Vickers hardness tester (Future Tech FM800) is used for hardness testing with a measuring parameter load of 1.96 N and a res-

Table 1
The actual chemical compositions of the original VZ232K powders and the LDED VZ232K as deposited sample (wt.%)

| Materials | Gd | Zn | Zr | Mg |
|---|---|---|---|---|
| Powders | 22.6 | 1.8 | 0.4 | Bal. |
| As deposited sample | 23.1 | 1.9 | 0.4 | Bal. |

idence time of 12 s. The Vickers hardness value is obtained by using 10 effective dots and removing the maximum and minimum values. The room-temperature stress-strain curves are obtained using an Instron 8801 material testing machine, with a tensile loading rate of 0.3 mm/min. The dimensions of the plate used for the tensile test are illustrated in Fig. 1 g. Room temperature tensile properties including yield strength (YS), ultra tensile strength (UTS) and elongation (EL) and the result is the average of at least three parallel tests. The fracture subsurface at the experiment after tensile experiment is observed by scanning electron microscopy.

## 3. Results

### 3.1. Microstructure characterization of as deposited alloy

As illustrated in Table 1, the detection results obtained by inductively coupled plasma emission spectrometer demonstrate that the bulk composition of the powder sample is Mg-22.6Gd-1.8Zn-0.4Zr. Following the deposition experiment, the composition of the as deposited sample is Mg-23.1Gd-1.9Zn-0.4Zr (referred to as VZ232K in this paper), which effectively reduces the evaporation loss problem of Mg element. The as-deposited VZ232K alloy exhibits a microstructure consisting of equiaxed grains with an average grain size of $11.9 \pm 2.1$ μm (Fig. 2a and b), which is notably smaller than those reported for the G20K alloy (16.1 μm) [24] and the GW103K alloy (19 μm) [25]. The inverse pole figure (IPF) map (Fig. 2b) demonstrates that the as-deposited VZ232K alloy has a uniform distribution multiplier of 1.98 for the base surface, indicating the absence of significant texture and a random grain orientation distribution. Microstructural analysis (Fig. 2d) reveals the presence of eutectic phases with a high area fraction (approximately 35.8%) exhibiting a characteristic reticular distribution. The addition of Zn is found to reduce the solid solubility of Gd in Mg, leading to the segregation of a substantial number of Gd atoms within the reticular eutectic phase. A higher-magnification SEM image (Fig. 2e) shows numerous fine precipitates distributed along the grain boundaries, whose structural and compositional characteristics require further investigation through TEM analysis.

Fig. 3 presents the crystal structure and compositional analysis of the precipitated and eutectic phases in the as-deposited VZ232K alloy. As shown in Fig. 3b and d, both the eutectic phase and the acicular precipitate phase demonstrate a crystal structure consistent with $Mg_3Gd$, adopting a face-centered cubic configuration with a lattice parameter of $a = 0.74$ nm. This structural configuration differs significantly from the $Mg_{24}Gd_5$ phase [25] typically observed in other Mg-Gd alloys. The high concentration of Gd atoms in the current system leads to an increased occupation of lattice sites by Gd atoms, thereby stabilizing the $Mg_3Gd$ crystal structure. STEM elemental mapping results (Fig. 3f) reveal significant enrichment of Gd and Zn atoms within the acicular precipitate phase, indicating preferential distribution of Zn in this phase. Based on these observations, the chemical composition of the acicular precipitate phase can be identified as $(Mg, Zn)_3Gd$.

### 3.2. Microstructure characterization of LDED-T4 alloy

The grain morphology, orientation distribution map and BSE-SEM maps of the second phase in the LDED-T4 VZ232K alloy are presented in Fig. 4. Following the solution heat treatment, grain growth is observed to be minimal, with an average grain size of only $16.1 \pm 2.6$ μm (Fig. 2b). The presence of the eutectic phase, which remains partially undissolved after the solution heat treatment, effectively inhibits grain boundary migration. As illustrated in Fig. 4c, the uniform distribution multiple of the basal plane is determined to be 1.98, indicating that the solution heat treatment does not significantly alter the basal plane texture. The area fraction of the eutectic phase, which undergoes substantial dissolution during the solution heat treatment, is measured at 12.5%. Additionally, the continuous reticular eutectic phase is transformed into isolated island-like eutectic phases. Within the grains, numerous clusters of needle-like phases are observed, with lengths ranging from 1 to 2 μm, as shown in the magnified image (Fig. 4e).

The LDED-T4 VZ232K alloy consists of a eutectic phase with a width of approximately 5 μm, a cluster needle-like phase and stacking fault structures (SFs) distributed throughout the entire grain, as shown in Fig. 5a. As depicted in Fig. 5b, the eutectic phase in the LDED-T4 VZ232K alloy retains the same crystal structure as the $Mg_3Gd$ phase. Notably, the eutectic phase undergoes only a reduction in area fraction after solid solution heat treatment, without any structural alteration. Elemental mapping analysis conducted in STEM mode (Fig. 5c and d) identifies the needle-like phase as a Zn-Zr constituent phase, which is similar to the $Zn_2Zr_3$ phase with a rosette-like structure previously reported in cast Mg-1Ca-1Zn-1Zr alloys [26].

Fig. 6 illustrates the crystal structure and high-resolution atomic morphology of the stacking faults (SFs) and long-period stacking ordered (LPSO) phases in the LDED-T4 VZ232K alloy. As shown in Fig. 6a, two distinct sizes of lamellar structural phases with parallel orientations are observed, along with a reduced number of LPSO phases and an increased number of SFs. The magnified bright-field image along the $[\bar{2}110]_\alpha$ direction (Fig. 6b) reveals that the lamellar structural phases are aligned perpendicular to the C* axis. Weak diffraction spots are observed between the $\alpha$-Mg diffraction spots in Fig. 6c. However, these additional spots do not correspond to the diffraction patterns of either type of LPSO phase. The high-resolution TEM image (Fig. 6d) highlights the size difference between the two lamellar structural phases, with the larger phase identified as the LPSO phase

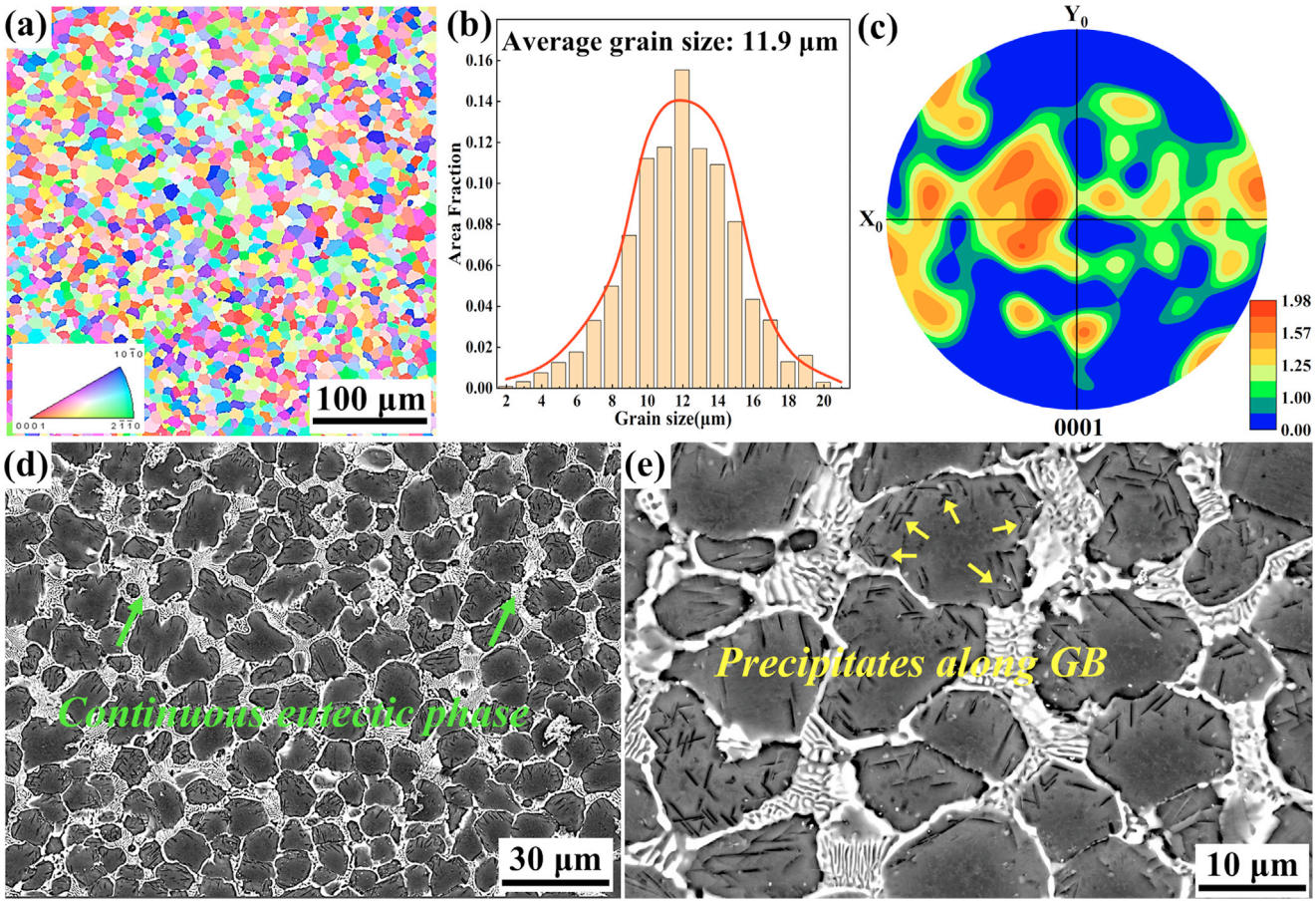


Fig. 2. As-deposited VZ232K alloy: (a) inverse pole figures (IPF); (b) grain size distribution; (c) pole figures; (d and e) BSE-SEM micrograph.

and the smaller phase classified as SFs along the C* axis. The results of the inverse fast Fourier transform (IFFT) (Fig. 6e) demonstrate that the atomic arrangement of the LPSO phase follows the AB|ABCA|CA|CA|C|B|AB|A stacking sequence characteristic of the 14H-LPSO structure. The period of SFs along the C* axis is <3.722 nm, indicating that SFs form during the early stages of the stable LPSO phase and represent a metastable LPSO structure. As shown in Fig. 6f, the stacking sequence of SFs aligns with the Frank partial dislocation model, with a Burgers vector $\mathbf{b} = 1/6 < 11\bar{2}0>$.

### 3.3. Modulus and hardness of as deposited alloy and LDED-T4 alloy

The distribution nephograms of the modulus and hardness of the microstructure, obtained by nanoindentation for the as-deposited alloy and the LDED-T4 alloy at a size of 50 × 50 μm, are presented in Fig. 7. The modulus and hardness of the α-Mg matrix in both the as-deposited alloy and the LDED-T4 alloy are significantly lower than those of the eutectic phase. The average modulus and hardness values of the matrix are 45 GPa and 1 GPa, respectively, while those of the eutectic phase are 65 GPa and 2.5 GPa, respectively. Following solution heat treatment, a slight increase in the modulus and hardness of the matrix is observed, reaching 48 GPa and 1.2 GPa, respectively. In contrast, a notable reduction in the modulus and hardness of the eutectic phase is observed, with values decreasing to 52 GPa and 1.5 GPa, respectively.

### 3.4. Aging hardening response and precipitation behavior of different aging conditions

To ultimately achieve superior mechanical properties, age hardening curves at 220 °C and 250 °C are established. As illustrated in Fig. 8a, the maximum hardness value of 144 Hv is attained at the peak aging condition of 220 °C for 12 h, which surpasses that of most rare-earth magnesium alloys. As the aging process progresses, the hardness of the alloy remains stable at 142 Hv up to 55 h. A second approximate plateau is observed during the 66 h to 100 h stage, with an average hardness of 138 Hv. The hardening curve at the aging temperature of 250 °C displays an approximate hardness plateau period followed by a gradual decline period. The plateau, with an average hardness of approximately 139 Hv, spans from 6 h to 60 h, while the gradual decline occurs from 60 h to 100 h. The results demonstrate that the peak aging time is shortened and the maximum hardness value decreases with increasing aging temperature. However, the duration of the hardness plateau is slightly extended, and the plateau transitions into a gradual hardness reduction in the later stages of aging.

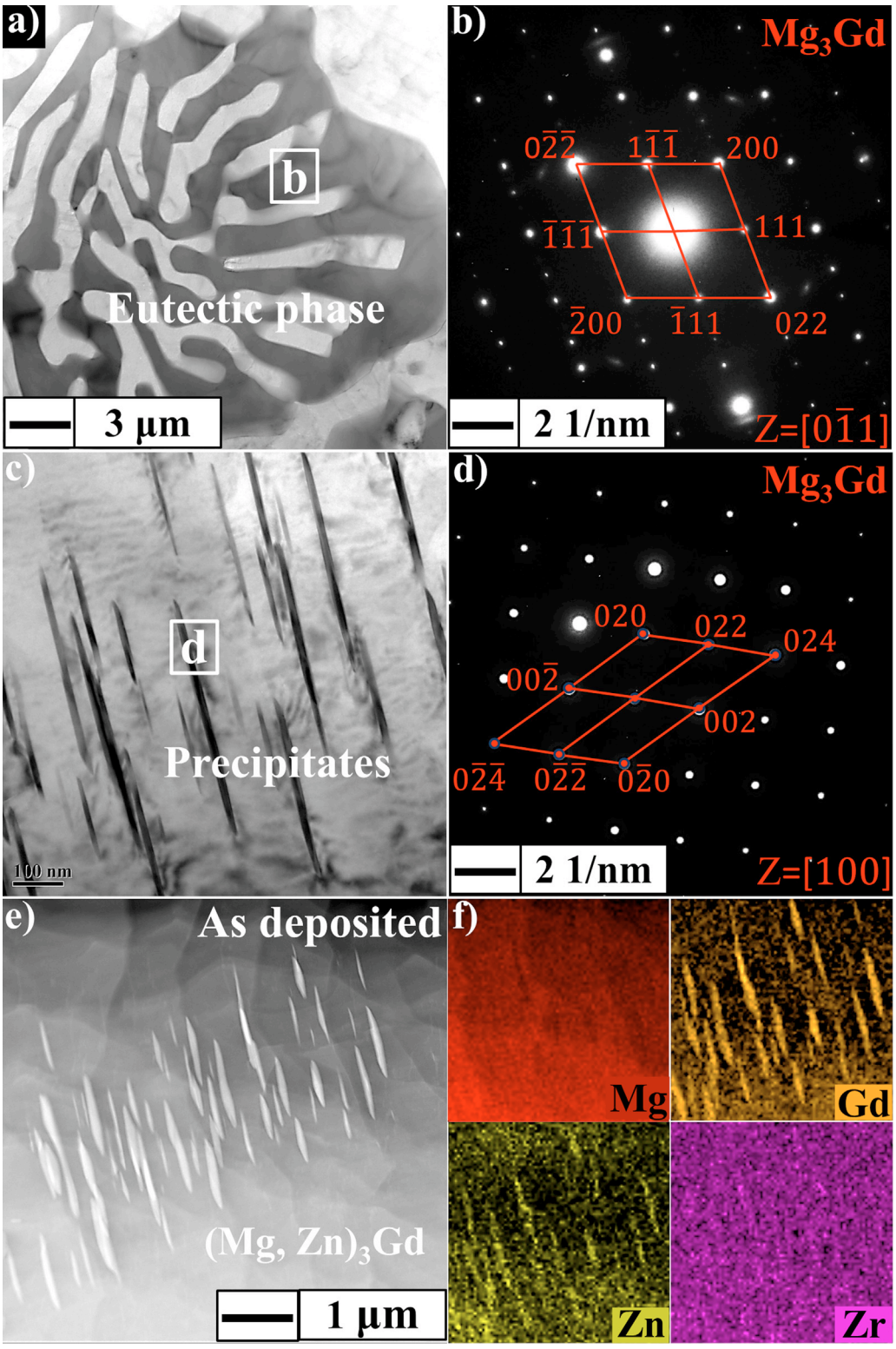


Fig. 3. TEM results for the morphology and crystal structure of the second phase of the as deposited VZ232K alloy: (a, b) eutectic phase; (c, d) acicular precipitate phase; (e, f) STEM results for acicular precipitated phase composition.

Fig. 9 illustrates the morphological evolution of the $\beta'$, $\beta_1$ and $\gamma'$ phases at different aging times at 220 °C. As shown in Fig. 9a, the stacking faults (SFs) throughout the grain are transformed into $\gamma'$ phase with a larger size (20–25 nm) after aging at 220 °C for 6 h. With increasing aging time, the width of the $\gamma'$ phase gradually decreases, and the $\gamma'$ phase remains perpendicularly aligned with the C* axis (Fig. 9e and g). A uniformly reticulated and finely densified $\beta'$ phase is

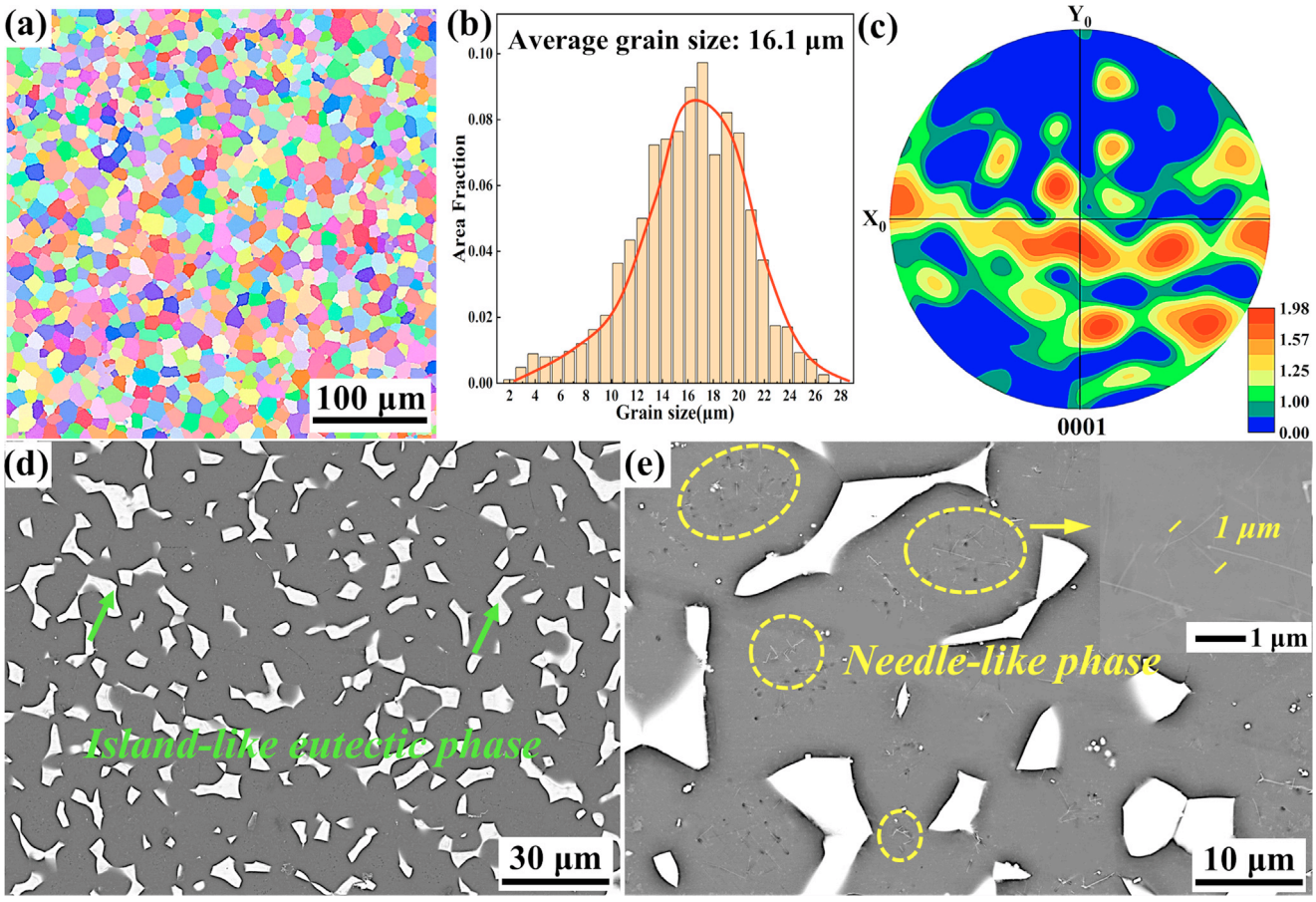


Fig. 4. LDED-T4 VZ232K alloy: (a) inverse pole figures (IPF); (b) grain size distribution; (c) pole figures; (d and e) BSE-SEM micrograph.

observed after aging at 220 °C for 12 h, with a length of 5.0–7.5 nm and a width of 4.5–6.0 nm. As depicted in Fig. 9f, the $\beta'$ phase transforms into a triangular configuration and lenticular morphology along the $\{1\bar{1}00\}_\alpha$ plane after aging at 220 °C for 55 h, with a length of 28–32 nm and a width of 7–9 nm. Two morphologies of the $\beta_1$ phase are formed at the necking regions of the $\beta'$ phase: one is initially nucleated, and the other is partially grown after nucleation. After aging at 220 °C for 100 h, lenticular $\beta'$ phases with a length of 30–35 nm and a width of 8–11 nm are observed, as shown in Fig. 9i. Compared to the peak aging state, the aspect ratio of the $\beta'$ phase shows a slight increase from 1.25 to 3.2. All electron diffraction patterns confirm that the precipitated phase under aging at 220 °C is a typical $\beta'$ phase, randomly distributed along the three $\{1\bar{1}00\}_\alpha$ directions.

Fig. 10 illustrates the morphological evolution of the $\beta'$ and $\beta_1$ phases at different aging times at 250 °C. Compared to the $\beta'$ phase observed at 220 °C for 12 h, the length of the $\beta'$ phase at 250 °C for 6 h increases by approximately 1–2 nm, while the width remains largely unchanged (Fig. 10b). The three-direction cross-interlocked structure of precipitated phases, formed at 220 °C for 55 h, is shown in Fig. 10c. A magnified view (Fig. 10d) reveals that this structure consists of a substantial $\beta'$ phase and a rhombic $\beta_1$ phase, which intersects the $\beta'$ phase obliquely at the neck. In comparison with the triangular configuration and lenticular $\beta'$ and $\beta_1$ phases observed at 220 °C for 55 h, the size of the $\beta'$ phase remains similar, while the size and number of $\beta_1$ phases slightly increase at 250 °C for 55 h. As depicted in Fig. 10e, the spacing within the three-direction cross-interlocked structure of precipitated phases progressively widens and thins. The length of the $\beta'$ phase increases to 55–70 nm, with a width of 12.5–15 nm, indicating that growth primarily occurs along the long axis, resulting in an increased aspect ratio of 4.6. Additionally, the number of rhombic $\beta_1$ phases intersecting the $\beta'$ phase obliquely at the neck increases to 2–3, while their size remains relatively unchanged.

### *3.5. Room temperature tensile properties and fracture subsurface morphology*

As shown in Fig. 11a, the ultimate tensile strength (UTS), yield strength (YS), and elongation (EL) of the as deposited LDED VZ232K alloy are 326 ± 4 MPa, 287 ± 3 MPa, and 2.1 ± 0.2%, respectively. The high yield strength of the as deposited alloy is attributable to fine grain strengthening. But a significant number of reticular eutectic phases, which function as the primary sites of crack initiation and propagation, result in a substantial reduction in elongation. The UTS, YS and EL of LDED-T4 VZ232K alloy are 308 ± 4 MPa, 221 ± 3 MPa, and 8.9 ± 0.4%, respectively. The optimal mechanical properties are observed at a temperature of

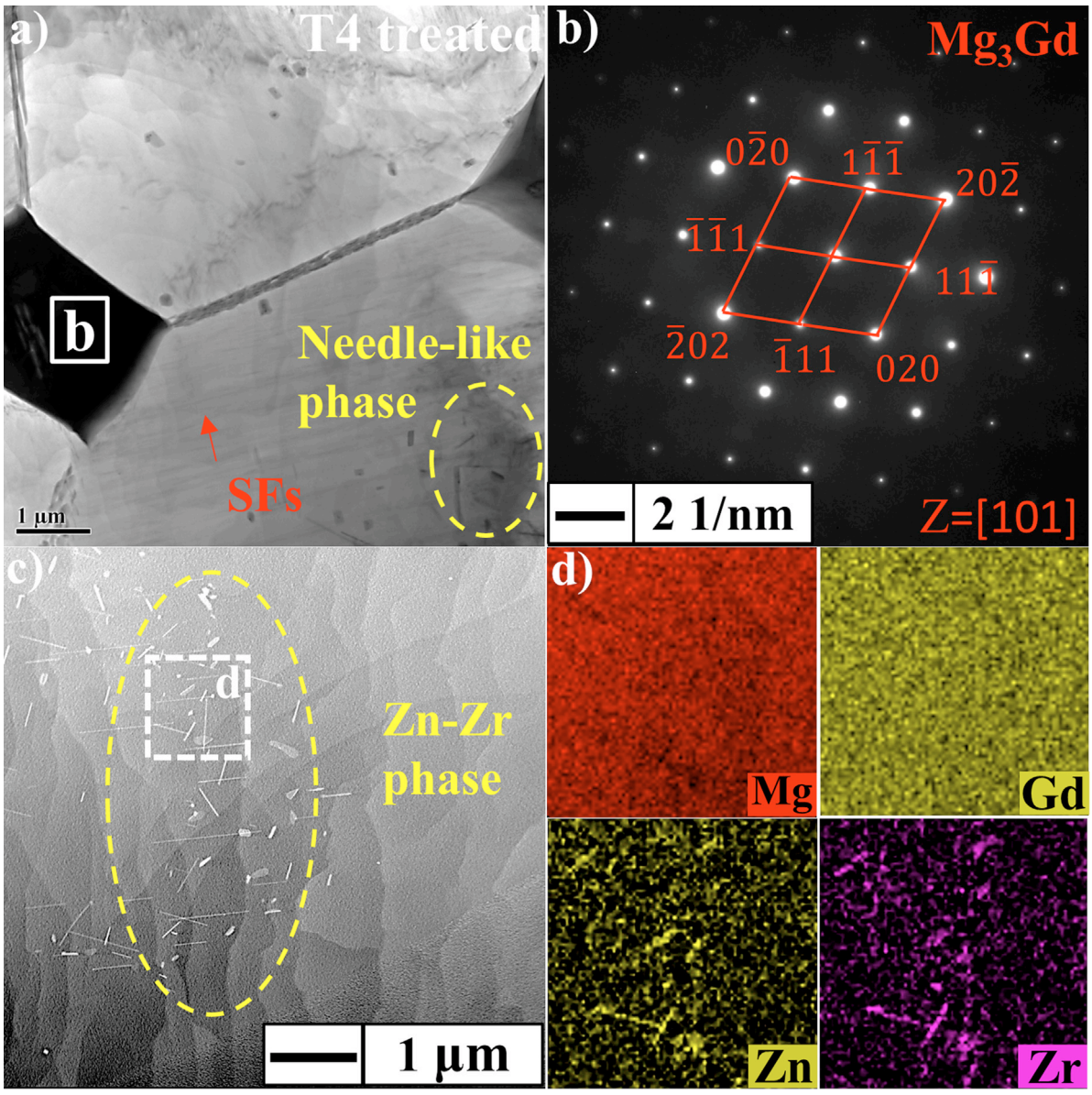


Fig. 5. (a, b) STEM diagram and EDS spectrum of the second phase of the T4 state alloy; (c) morphology at grain boundaries; (d) STEM results for Zn-Zr phase composition.

T61–220 °C for 12 h, resulting in an UTS of 424 ± 6 MPa, a YS of 326 ± 4 MPa, and an EL of 3.4 ± 0.2%, respectively.

Fig. 12 presents the fracture subsurface backscattering scanning electron microscopy (BSEM) images along with the crack propagation mechanism diagram. In the as-deposited alloy, the crack initiation is observed to originate from the hard and brittle eutectic phase, with crack propagation occurring along interconnected eutectic phases at the grain boundaries, as depicted in Fig. 12a. The interconnected reticular eutectic phase within the as-deposited alloy provides an effective pathway for crack propagation, ultimately exhibiting characteristics typical of intergranular fracture. For the LDED-T4 alloy, a significant number of secondary cracks are observed within the isolated eutectic regions, as illustrated in Fig. 12b. The presence of these secondary cracks suggests that the isolated eutectic phase undergoes substantial deformation, and the high density of stacking faults within the $\alpha$-Mg matrix further enhances the deformability of the LDED-T4 alloy. Consequently, the ductility of the LDED-T4 VZ232K alloy is markedly improved, and the fracture mode transitions from intergranular to transcrystalline, as shown in Fig. 12c. For the LDED-T6 alloy, the stacking faults (SFs) transform into larger $\gamma'$ phases with reduced coordinated deformability following aging heat treatment, as demonstrated in Fig. 12d. As a result, the LDED-T6 alloy exhibits a mixed fracture mode, combining both intergranular and transcrystalline fracture characteristics.

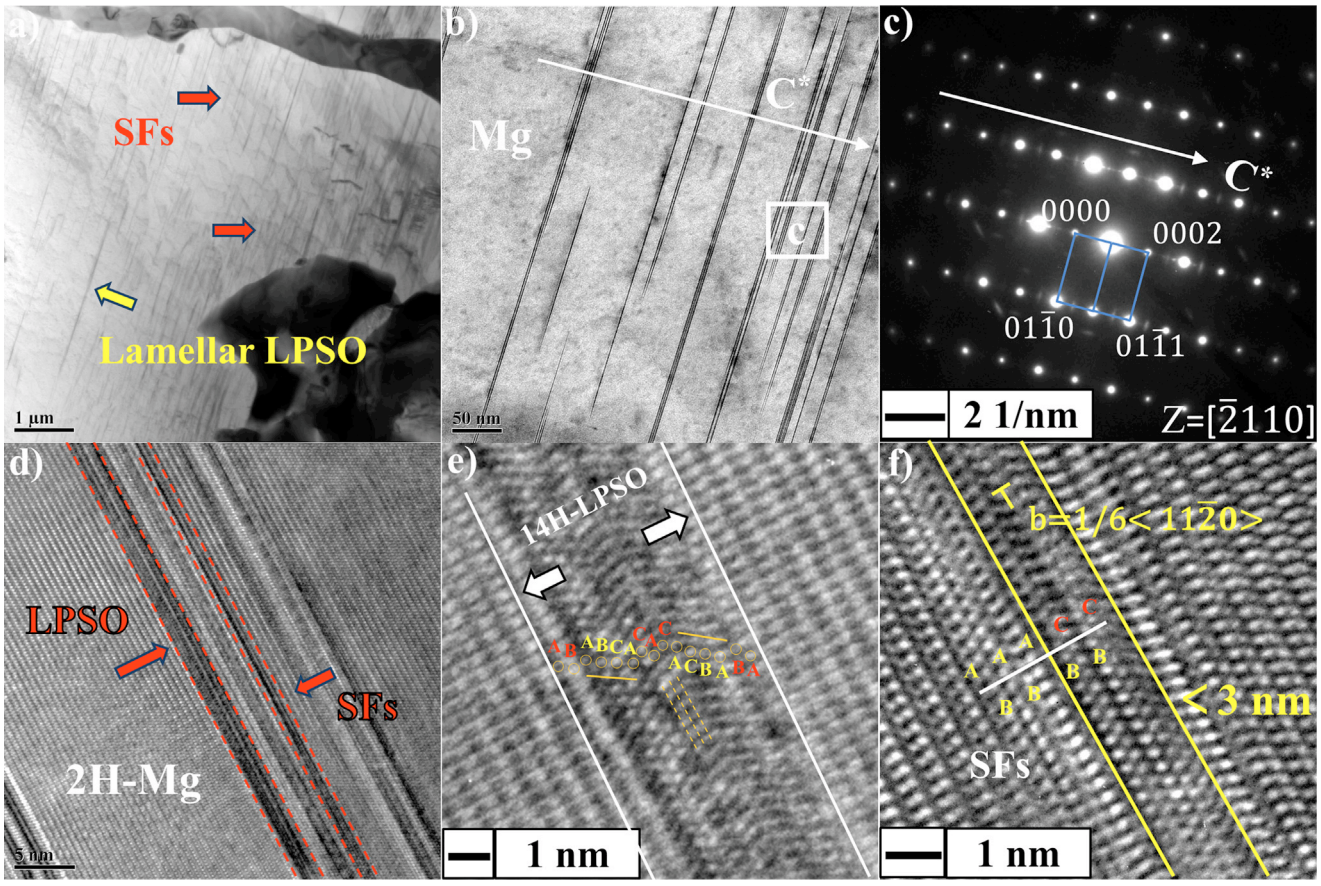


Fig. 6. TEM results for the LDED-T4 VZ232K alloy: (a, b) bright field image; (c) SAED of SFs; (d) HRTEM image of the lamellar SFs and LPSO phase; (e, f) IFFT of LPSO phase and SFs.

Table 2
As deposited grain size of Mg-Gd alloy under different processes

| Composition | Process | Grain size | Ref. |
|---|---|---|---|
| VZ232K | L-DED | 11.9 μm | This work |
| GW93K | L-DED | 12 μm | [9] |
| GW103K | L-DED | 19 μm | [39] |
| GW63K | W-DED | 12.7 μm | [25] |
| GWZ1031K | W-DED | 22.3 μm | [35] |
| GWZ932K | W-DED | 11.6 μm | [40] |
| GWZ941K | W-DED | 39.3 μm (NRZ)<br>26.8 μm (RMZ) | [30] |
| GWQ832K | Cast | 31 μm | [38] |
| GZ171K | Cast | 30 μm | [41] |
| G15K | Cast | 41 μm | [42] |
| GZ151K | Cast | 29 μm | |
| GZ121K | Cast | 71 μm | [43] |
| GW63K | Cast | 45 μm | [44] |

## 4. Discussion

### *4.1. Effects of ultra-high gd content on microstructure and mechanical properties of as deposited, solution and peak aging states*

As illustrated in Fig. 13 and Table 2, the LDED-VZ232K alloy exhibits a smaller equiaxed grain size compared to conventional cast magnesium alloys and direct energy deposition (DED) Mg-Gd alloys with lower Gd content. In contrast to conventional casting, LDED technology is characterized by layer-by-layer scanning and higher heat input, leading to a faster cooling rate and finer grain formation. During solidification, high-Gd alloys demonstrate enhanced compositional undercooling of the liquid phase at the solid-liquid interface front and greater grain refinement compared to low-Gd specimens. Additionally, the significant enrichment of rare earth elements (REEs) at grain boundaries further

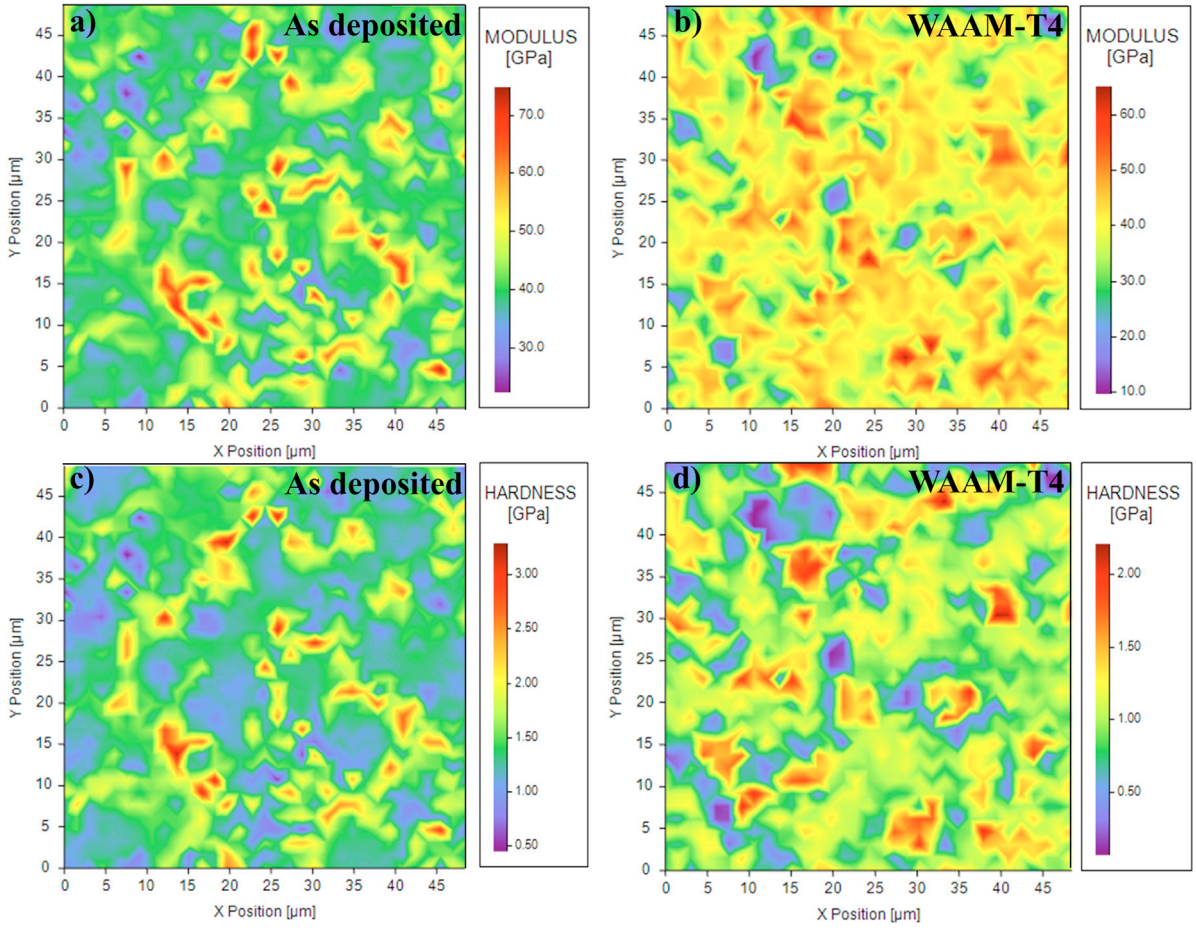


Fig. 7. (a) modulus and (c) hardness distribution nephogram of the as deposited alloy; (b) modulus and (d) hardness distribution nephogram of LDED-T4 alloy.

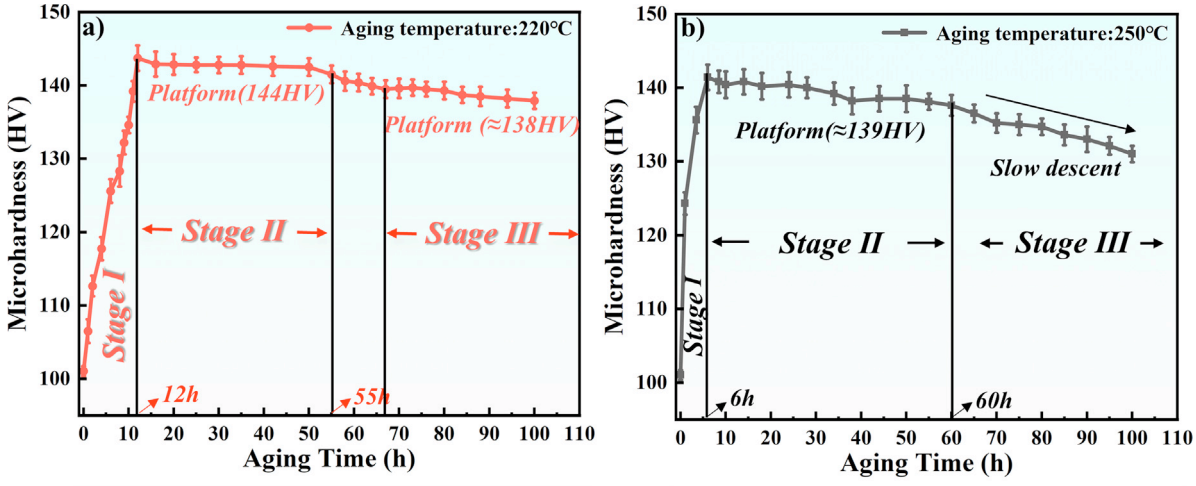


| | Under aging | Peak aging | Over aging | Over aging |
|---|---|---|---|---|
| Time(h) | 6 | 12 | 55 | 100 |
| Hardness(HV) | 125±1 | 144±3 | 142±3 | 138±2 |

| | Peak aging | Over aging | Over aging | Over aging |
|---|---|---|---|---|
| Time(h) | 6 | 34 | 60 | 100 |
| Hardness(HV) | 141±2 | 140±2 | 138±2 | 131±2 |

Fig. 8. Aging hardening curve of VZ232K alloy: (a) 220 °C; (b) 250 °C.

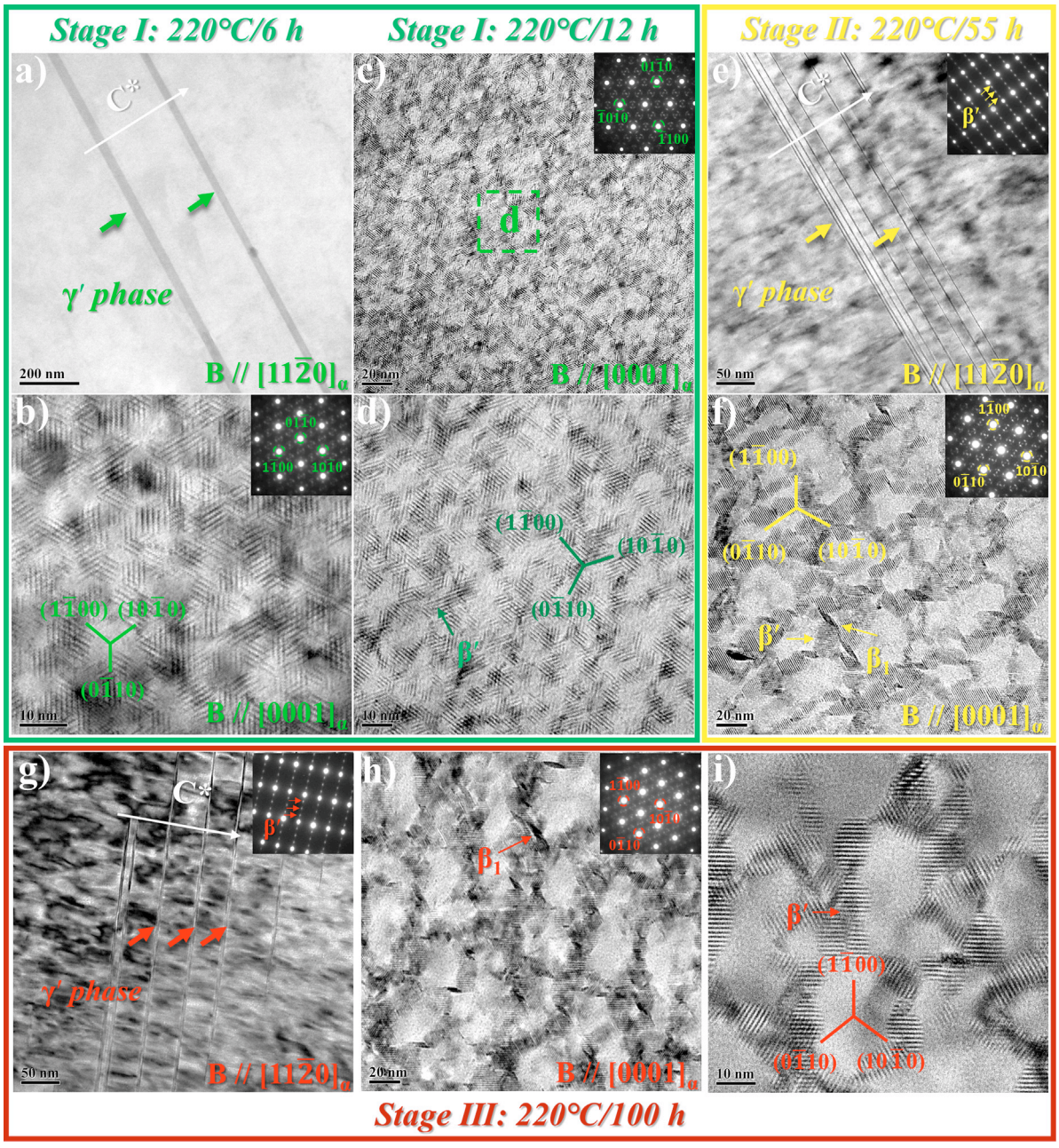


Fig. 9. TEM images and SAED plots of LDED-T6 VZ232K alloy: (a, b) 220 °C for 6 h; (c, d) 220 °C for 12 h; (e, f) 220 °C for 55 h; (g, h, i) 220 °C for 100 h;.

inhibits grain growth. According to the Hall-Petch relationship: $\sigma_{GB} = k_y d^{-\frac{1}{2}}$ (1), it is evident that a smaller grain size contributes to a stronger grain boundary strengthening effect, which is the primary reason for the higher yield strength of the as-deposited alloy. In this study, no long-period stacking ordered (LPSO) phase is observed in the as-deposited LDED-VZ232K alloy. However, after heat treatment at 500 °C for 8 h, a large number of stacking faults (SFs) and a small amount of lamellar LPSO phase are formed within the grains. The possible reasons for this formation are as follows:

Previous studies have indicated that the ratio of rare earth (RE) atoms to Zn atoms, the cooling rate and the heat treatment regime significantly influence the formation of the long-period stacking ordered (LPSO) phase. In the as-cast GWZ1041 alloy [5], the needle-like structure was identified as stacking faults (SFs), whereas in the GWZ1042 alloy, this structure transforms into the LPSO phase. No LPSO phase was observed in the as-deposited VZ112K alloy [27] under the laser powder bed fusion (LPBF) process, which was characterized by a high cooling rate. However, a significant number of lamellar 14H-LPSO phases formed after solution heat treatment at 400–480 °C. These findings suggest that a high cooling rate or a high atomic ratio of rare earth to Zn (denoted as λ) is unfavorable for the formation of the LPSO phase.

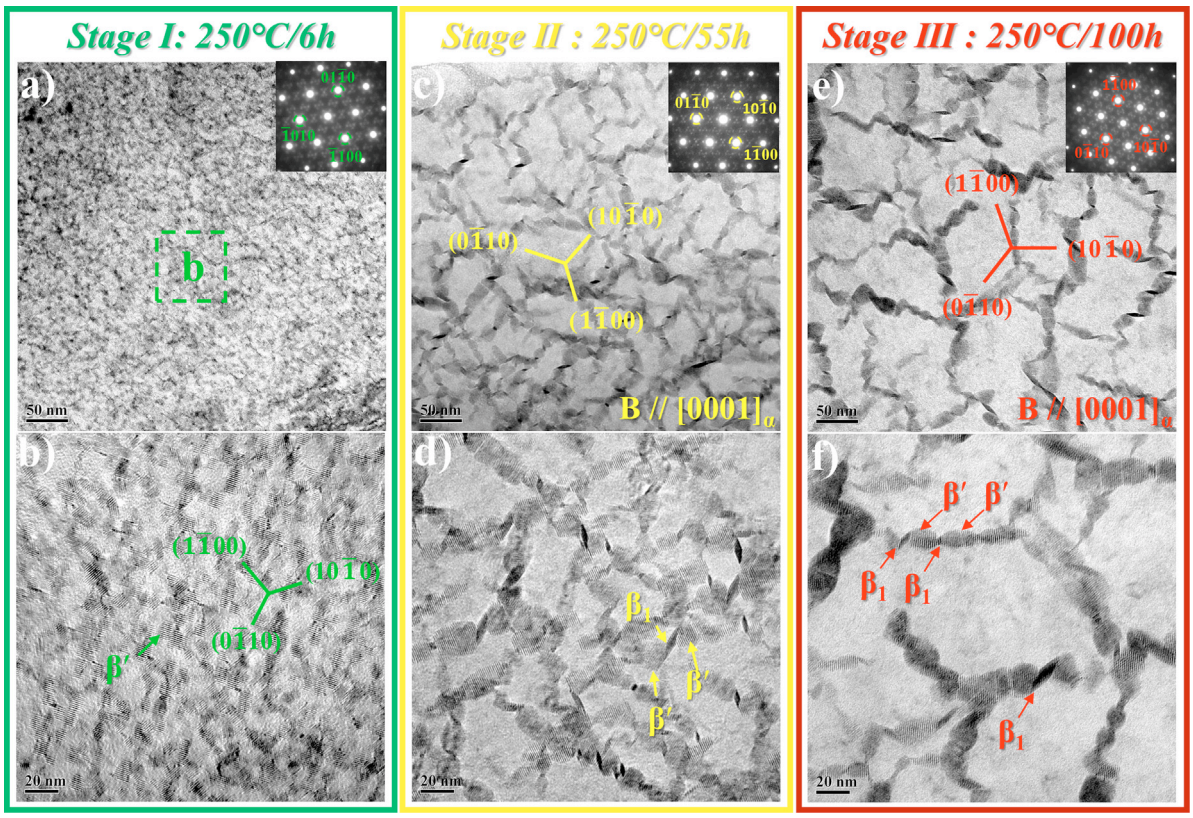


Fig. 10. TEM images and SAED plots of LDED-T6 VZ232K alloy: (a, b) 250 °C for 6 h; (c, d) 250 °C for 55 h; (e, f) 250 °C for 100 h.

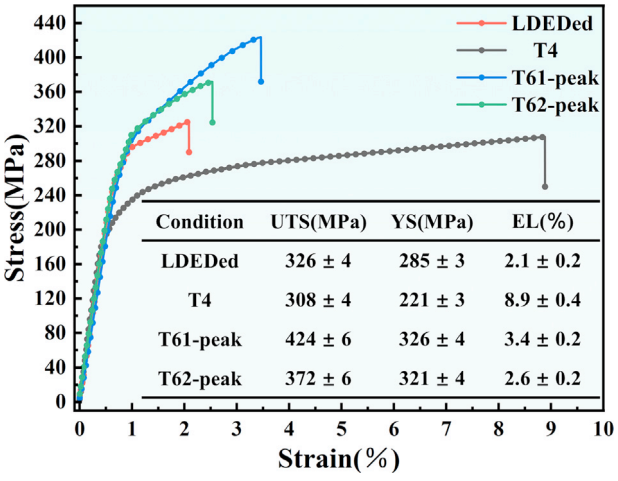


Fig. 11. Room temperature tensile properties of LDED VZ232K alloy under different heat treatment regimes.

Although the cooling rate of the LDED process in this study is lower than that of the LPBF process, the higher λ value (4.8) ensures that the as-deposited alloy does not meet the necessary conditions for the compositional ordering required for LPSO phase formation.

The solution heat treatment process effectively reduces the stacking fault energy and promotes the decomposition of full dislocations into stacking faults and partial dislocations [28]. During thermal diffusion, Gd and Zn atoms segregate into specific stacking fault regions, facilitating the slip of partial dislocations and promoting the expansion and growth of these regions, thereby forming the LPSO phase. This process requires a lower λ value, which is not satisfied in the LDED VZ232K alloy due to its higher λ value. Consequently, the expansion of stacking fault regions is hindered, and only the decomposition of full dislocations into stacking faults occurs. As a result, numerous SFs and a small number of fine lamellar 14H-LPSO phases coexist. The obstruction effect on dislocation slip is directly proportional to the size of the LPSO phase. However, larger LPSO phases are also prone to stress concentration, which can reduce ductility [29]. In this study, the carefully designed heat treatment process (employing a lower heat treatment temperature) effectively minimizes the formation of large LPSO phases. The coordination of plastic deformation within the grains is achieved through small-sized SFs and extremely fine lamellar LPSO phases, thereby maintaining ductility while enhancing strength for subsequent aging heat treatment.

Appropriate low-temperature aging heat treatment is an effective approach to enhancing the strength of Mg-Gd alloys. Previous studies have indicated that the optimal aging heat treatment temperature for medium- or low-rare-earth-element (REE) magnesium alloys typically ranges between 170 °C and 220 °C [23]. In this study, magnesium alloys with high Gd content demonstrate improved hardness and superior strength (Fig. 11) under peak aging conditions at 220 °C and 250 °C. Numerous studies focusing on the quantitative calculation of

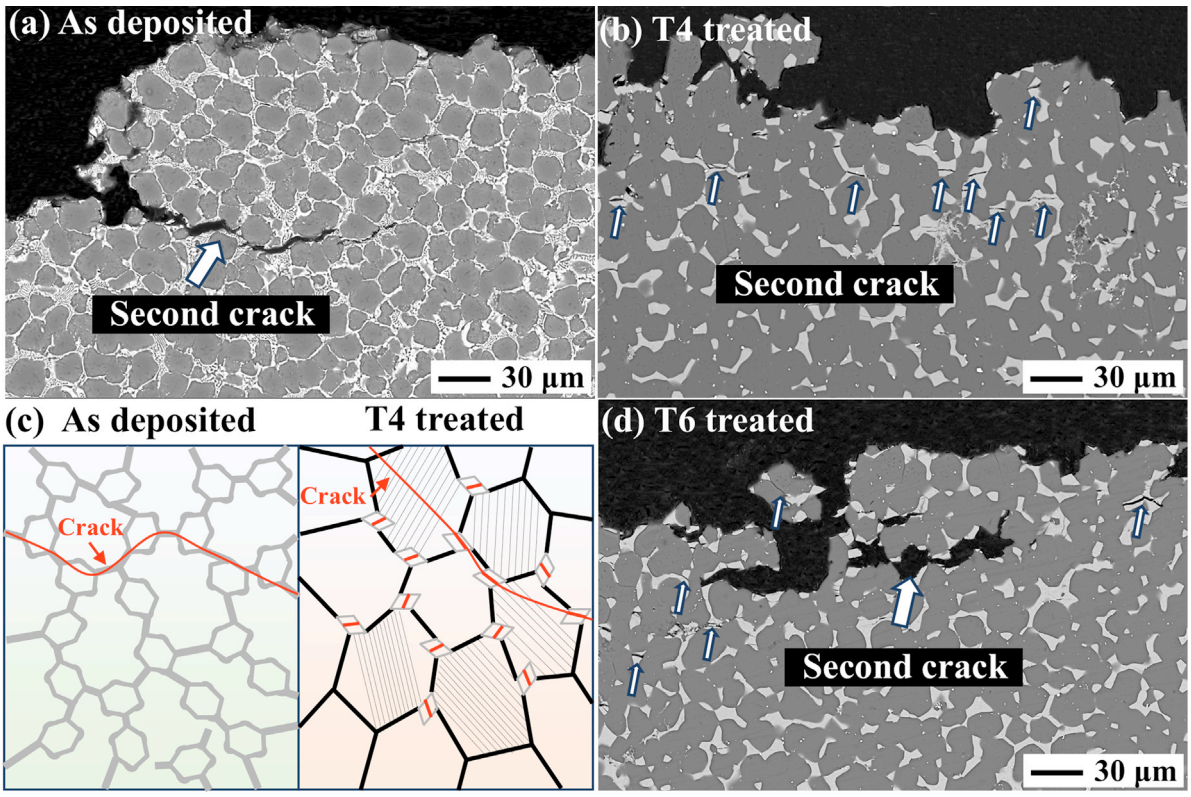


Fig. 12. Fracture subsurface of LDED VZ232K alloy in different heat-treated states: (a) as deposited alloy; (b) LDED-T4; (c) fracture mechanism of as deposited and T4 treated alloys;(d) LDED-T6.

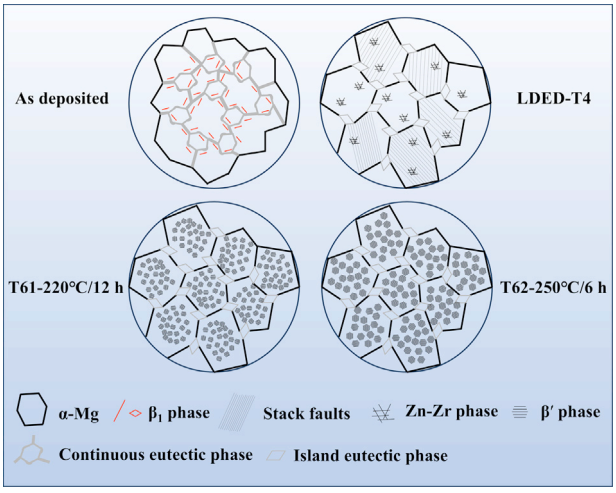


Fig. 13. Microstructure evolution mechanism diagram of LDED VZ232K alloy in different heat treatment states.

yield strength contributions in magnesium alloys [12,30,31] have shown that the precipitation of the $\beta'$ phase contributes >50% to the overall strength, representing the predominant strengthening mechanism. The $\beta'$ phase primarily enhances strength by impeding basal dislocation slip. The relationship between the yield strength resulting from precipitation strengthening and the characteristics of strengthening particles can be described using the Orowan equation [32].

$$\Delta\sigma_{Orowan} = \frac{2Gb}{d}\left(\frac{6f}{\pi}\right)^{1/3} \quad (2)$$

where G is the shear modulus (16.5 GPa), b is the Burr's vector (0.32 nm) [33], d is the diameter of the $\beta'$ phase, and f is the average volume fraction of the $\beta'$ phase. Quantitative measurement of the volume fraction of the $\beta'$ phase is challenging and often lacks precision. It is widely accepted that the number density of the $\beta'$ phase exhibits a positive correlation with its volume fraction. Therefore, the following discussion will use the number density as a proxy for the volume fraction. According to Eq. (2), it can be inferred that an increase in the number density of the $\beta'$ phase and a reduction in its diameter can enhance the yield strength. The number densities, lengths, widths and yield strength values of the $\beta'$ phases in Mg-Gd alloys under peak aging conditions, as reported in the literature, are summarized in Table 3. The number density is calculated as the number of $\beta'$ phases satisfying the three variant orientations divided by the actual area of the published micrograph. The $\beta'$ phase number density of the LDED-T6 VZ232K alloy is approximately $2.4 \times 10^4$ $\mu m^{-2}$, which is 2–6 times higher than that of other high-REE magnesium alloys subjected to solution and aging heat treatment. Additionally, the dimensions of the peak-aged $\beta'$ phase in the LDED-T6 VZ232K alloy, both in length and width, are the smallest compared to those of other Mg-Gd alloys. On the one hand, the strengthening effect of the alloy

Table 3
the $\beta$' phase number density, length, thickness, hardness and yield strength of heat-treated Mg-Gd magnesium alloys under peak aging state have been published.

| Process and Composition | Aging regime | Number density ($\mu m^{-2}$) | Length (nm) | Width (nm) | YS (MPa) | Ref. |
|---|---|---|---|---|---|---|
| LDED-VZ232K | 220 °C for 12 h | $1.7 \times 10^4$ | 6.4 | 5.5 | 326 | This work |
| | 220 °C for 55 h | $5.4 \times 10^3$ | 30.2 | 7.8 | 311 | |
| | 220 °C for 100 h | $5.1 \times 10^3$ | 32.3 | 9.4 | 310 | |
| LDED-VZ232K | 250 °C for 6 h | $1.6 \times 10^4$ | 7.5 | 5.9 | 321 | |
| | 250 °C for 55 h | $5.2 \times 10^3$ | 31.5 | 8.2 | 307 | |
| | 250 °C for 100 h | $8.8 \times 10^2$ | 61.3 | 13.7 | 303 | |
| LPBF-GWZ1221M | 175 °C for 256 h | $1.1 \times 10^4$ | 7.8 | 6.5 | 320 | [20] |
| WAAM-GW93K | 225 °C for 16 h | $1.3 \times 10^4$ | 9.8 | 6.2 | 262 | [21] |
| LPBF-VZ112K | 175 °C for 256 h | $4.1 \times 10^3$ | 8.1 | 5.6 | 343 | [27] |
| LPBF-GWZ1031K | 200 °C for 64 h | $6.6 \times 10^3$ | 7.8 | 6.5 | 323 | [34] |
| WAAM-GW63K | 200 °C for 80 h | $9.9 \times 10^3$ | 6.6 | 5.7 | 218 | [25] |
| Cast-G12K | 225 °C for 2 h | $2.6 \times 10^3$ | 7.9 | 5.5 | 221 | [43] |
| | 225 °C for 8 h | $3.7 \times 10^3$ | 8.6 | 5.6 | 231 | [43] |
| | 225 °C for 32 h | $1.3 \times 10^3$ | 17.1 | 9.1 | 243 | [43] |
| Cast-G1204K | 225 °C for 2 h | $1.6 \times 10^3$ | 6.5 | 5.2 | 181 | [43] |
| | 225 °C for 8 h | $2.9 \times 10^3$ | 8.7 | 5.6 | 229 | [43] |
| | 225 °C for 32 h | $1.5 \times 10^3$ | 14.6 | 10.1 | 252 | [43] |
| Cast-G1208K | 225 °C for 2 h | $1.2 \times 10^3$ | 5.5 | 4.4 | 171 | [43] |
| | 225 °C for 8 h | $1.4 \times 10^3$ | 12 | 7.8 | 273 | [43] |
| | 225 °C for 32 h | $1.0 \times 10^3$ | 15.2 | 11.1 | 267 | [43] |

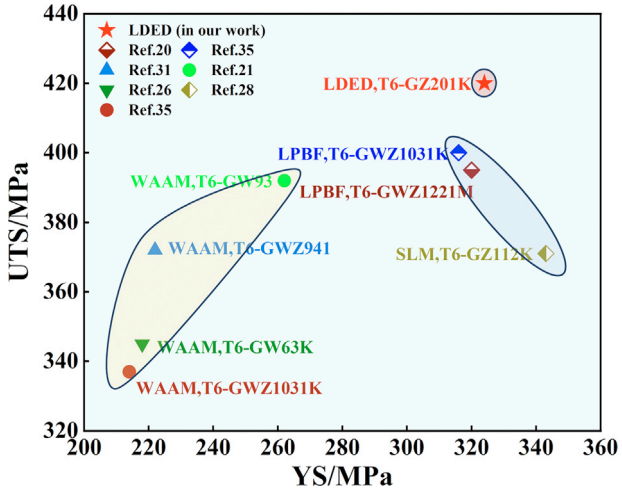


Fig. 14. Comparison of room temperature tensile properties between LDED-T6 VZ232K alloy and other additive manufactured T6 Mg-Gd alloys.

is enhanced by the increased number density of the $\beta'$ phases. On the other hand, the smaller dimensions in both length and width directions result in a reduced d, further contributing to the improvement in yield strength. These results demonstrate that, compared to other Mg-Gd alloys with high Gd content, the LDED VZ232K alloy exhibits a higher $\beta'$ phase number density and smaller phase dimensions, highlighting the significant precipitation strengthening effect in ultra-high Gd alloys. Fig 14

In this study, the peak tensile strength and yield strength of the LDED VZ232K alloy were compared with those of other Mg-Gd alloys [20,21,25,27,30,34,35] with medium and high Gd content following solution and aging heat treatment. The overall mechanical properties of the LDED-T6 VZ232K alloy reported in this work are superior, exhibiting the highest tensile strength and the second-highest yield strength. Although the LPBF-T6 high-REE magnesium alloy possesses a finer grain size, its yield strength is slightly lower than that of the LDED-T6 VZ232K alloy. This discrepancy can be attributed to the stronger second-phase strengthening, solid solution strengthening from rare earth (RE) atoms, and precipitation strengthening effects of high-density nano-precipitated phases in the LDED-T6 VZ232K alloy compared to the LPBF-T6 high-REE magnesium alloy. While the grain size of the high-Gd-content Mg-Gd alloy in DED-T6 is similar to that of the LDED-T6 VZ232K alloy, the former demonstrates weaker performance in the other three major strengthening mechanisms relative to the latter. The successful fabrication of ultra-high rare earth content alloys using the LDED process highlights its unique advantages over other manufacturing techniques.

### *4.2. Effect of ultra-high gd content on microstructure and mechanical properties of over aging state*

The $\beta'$ phase in the over-aging state exhibits two distinct characteristics. First, it maintains a high number density. Second, it forms a three-directional cross-interlocked structure, as illustrated in Fig. 15. The ultra-high Gd content reduces the nucleation barrier of the $\beta'$ phase in the supersaturated solid solution, significantly enhancing the uniform nucleation rate and resulting in the formation of an ultra-high-density $\beta'$ phase ($1.7 \times 10^4$ $\mu m^{-2}$) during the early stages of aging. The three-directional cross-interlocked structure can be interpreted as a transformation of the $\beta'$ phase from a spherical morphology with a low aspect ratio to a sheet-like morphology with a high aspect ratio. The morphology of the precipitated phase is primarily governed by the balance between interface energy

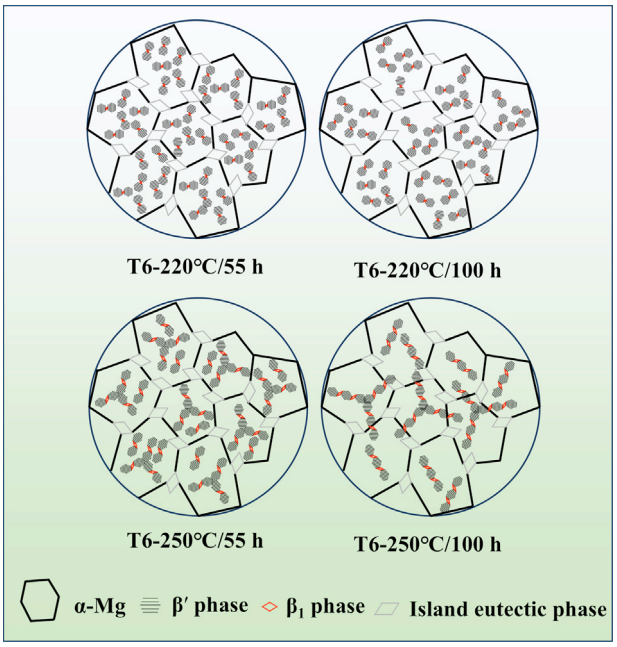


Fig. 15. Microstructure evolution mechanism diagram of LDED VZ232K alloy in overaged state.

and strain energy. The expressions for strain energy, denoted as $\Delta G_\varepsilon$, and interface energy, denoted as $\Delta G_\sigma$, are as follows:

$$\Delta G_\varepsilon = \frac{4}{3}\pi r^3 \varepsilon \tag{3}$$

$$\Delta G_\sigma = 4\pi r^2 \sigma \tag{4}$$

Where r is the particle diameter of the precipitated phase, $\varepsilon$ is the unit strain energy, and $\sigma$ is the unit interface energy. Assuming that $\varepsilon$ and $\sigma$ are close, it can be considered that the interfacial energy resistance ($\Delta G_\sigma$) is greater than the strain energy resistance ($\Delta G_\varepsilon$) at the initial nucleation stage. As a result, the spherical morphology of the initial $\beta'$ phase is favored to minimize the interfacial energy resistance. However, as the size of the $\beta'$ phase increases beyond a critical threshold, the strain energy ($\Delta G_\varepsilon$) becomes more significant than the interfacial energy resistance ($\Delta G_\sigma$). Consequently, the $\beta'$ phase transitions to a sheet-like morphology, which reduces the strain energy. The growth of the $\beta'$ phase along the three prismatic planes, when projected onto the basal plane, results in the formation of a three-directional cross-interlocked structure.

The room temperature tensile test results for four sets of over-aged specimens are presented in Fig. 16. The ultimate tensile strength and elongation of the alloy decrease to some extent with prolonged aging time, while the reduction in yield strength is less pronounced, remaining above 300 MPa. In contrast to other low-content Mg-Gd alloys, where significant coarsening and growth of the precipitated phase under over-aging conditions can detrimentally affect yield strength, the $\beta'$ phase in the LDED-T6 VZ232K alloy undergoes a transition from a uniformly reticulated distribution to a three-directional

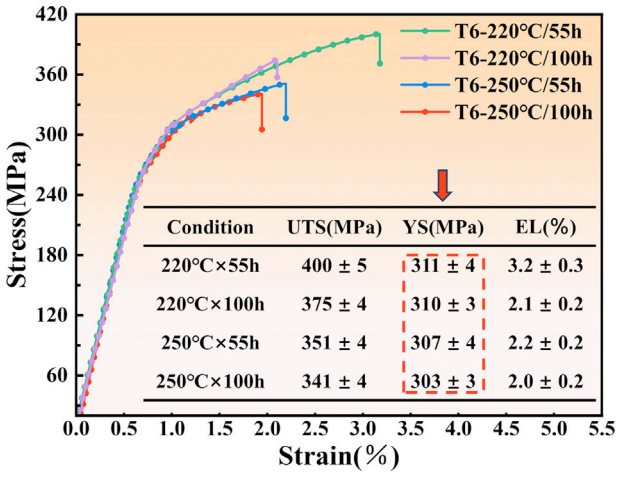


| Condition | UTS(MPa) | YS(MPa) | EL(%) |
|---|---|---|---|
| 220°C×55h | 400 ± 5 | 311 ± 4 | 3.2 ± 0.3 |
| 220°C×100h | 375 ± 4 | 310 ± 3 | 2.1 ± 0.2 |
| 250°C×55h | 351 ± 4 | 307 ± 4 | 2.2 ± 0.2 |
| 250°C×100h | 341 ± 4 | 303 ± 3 | 2.0 ± 0.2 |

Fig. 16. Room temperature tensile properties at 220 °C and 250 °C.

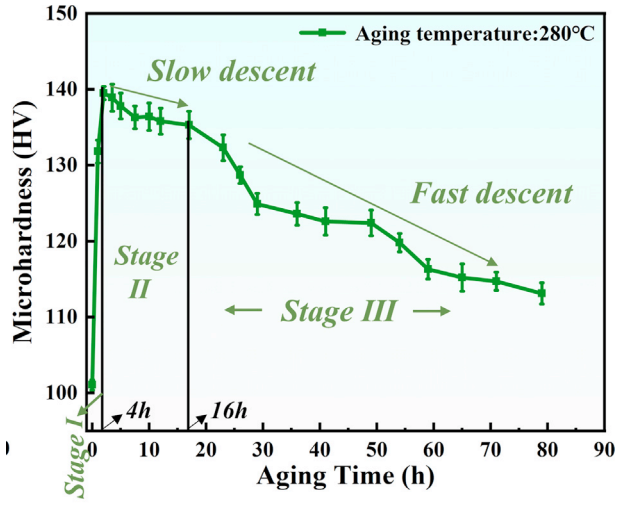


| | Peak aging | Over aging | Over aging | Over aging |
|---|---|---|---|---|
| Time(h) | 4 | 16 | 55 | 80 |
| Hardness(HV) | 140±2 | 136±2 | 120±2 | 113±2 |

Fig. 17. Aging hardening curve of VZ232K alloy at 280 °C.

cross-interlocked structure during the over-aging stage. Previous studies [36] have consistently demonstrated that the $\beta'$ phase with a three-directional cross-interlocked structure possesses a larger surface area capable of impeding dislocation slip compared to the unidirectional $\beta'$ phase, thereby exerting a more pronounced effect on yield strength enhancement. Therefore, it can be inferred that the retention of high and stable yield strength in the over-aged state is likely attributed to the $\beta'$ phase with its higher and stable number density (as shown in Table 3) and the three-directional cross-interlocked structure.

The LDED-T6 VZ232K alloy demonstrates a distinct elevated hardness plateau under over-aging conditions, a phenomenon rarely observed in other Mg-Gd alloys with lower Gd content. Numerous studies [23,37] have shown that increasing the aging temperature reduces the time required to

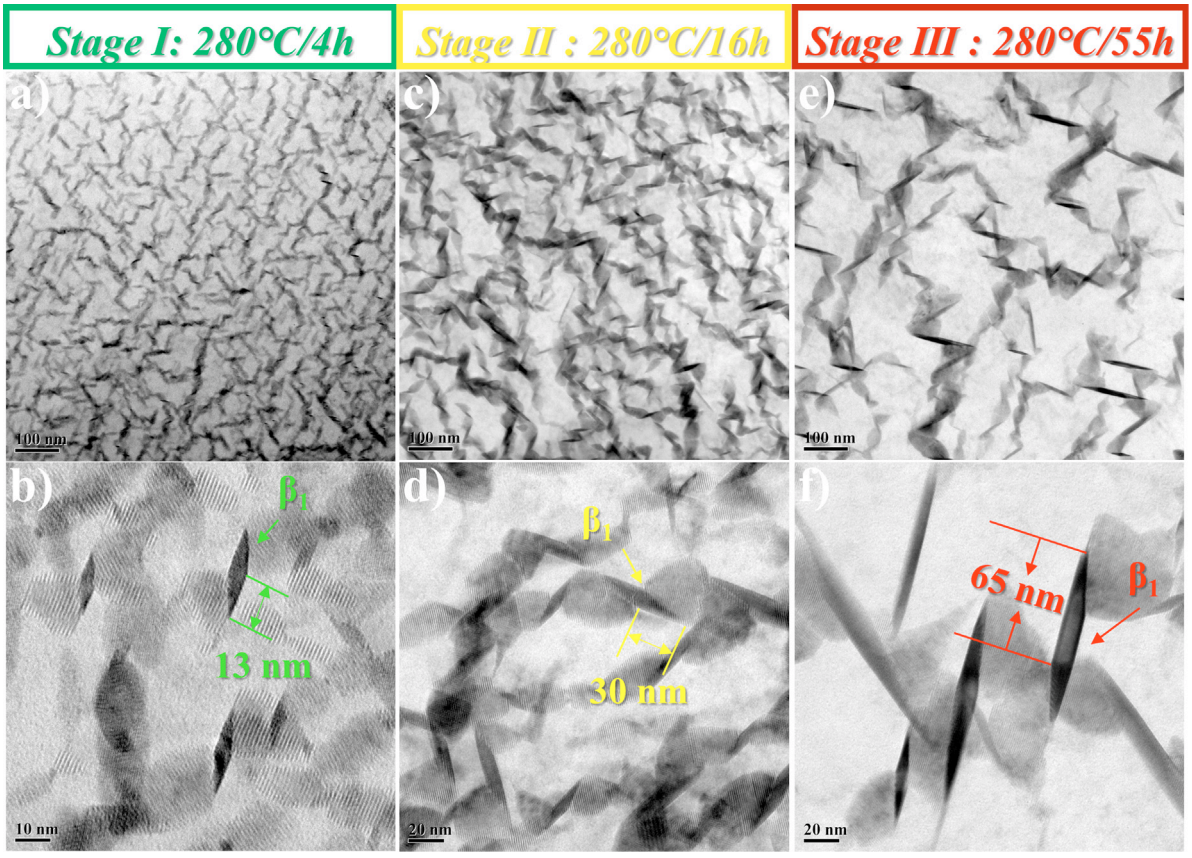


Fig. 18. TEM image of LDED-T6 VZ232K alloy:(a, b) 280 °C for 4 h; (c, d) 280 °C for 16 h; (e, f) 280 °C for 55 h.

Table 4
Hardness and duration of heat-treated Mg-Gd magnesium alloys in the published aging state

| Process and Composition | Aging regime | Hardness | Plateau time | Ref. |
|---|---|---|---|---|
| LDED-T61 VZ232K | Over-220 °C for 55 h | 144 Hv | 43 h | This work |
| | Over-220 °C for 100 h | 138 Hv | 40 h | |
| LDED-T62 VZ232K | Over-250 °C for 55 h | 140 Hv | 64 h | |
| | Over-250 °C for 100 h | 131 Hv | 30 h | |
| WAAM-T6 GW93K | Peak-225 °C for 16 h | 126 Hv | 14 h | [21] |
| | Over-225 °C for 96 h | 118 Hv | 20 h | |
| LPBF-T6 GWZ1221M | Peak-175 °C for 256 h | 130 Hv | 0 | [20] |
| | Peak-200 °C for 32 h | 128 Hv | 40 h | |
| WAAM-T6 GW63K | Peak-200 °C for 80 h | 114 Hv | | [25] |
| LPBF-T6 GWZ1031K | Peak-200 °C for 64 h | 131 Hv | 0 | [34] |
| | Peak-175 °C for 256 h | 133 Hv | 56 h | |
| LPBF-T6 GZ112K | Peak-175 °C for 256 h | 115 Hv | 0 | [27] |
| | Peak-200 °C for 64 h | 110 Hv | 0 | |
| WAAM-T6 GWZ941K | Peak-200 °C for 128 h | 125 Hv | 0 | [30] |
| Cast-T6 GWQ832K | Peak-175 °C for 292 h | 135 Hv | 0 | [38] |
| | Peak-200 °C for 32 h | 128 Hv | 60 | |
| | Peak-225 °C for 12 h | 120 Hv | 40 | |
| Cast-T6 GZ171K | Peak-225 °C for 24 h | 138 Hv | 10 | [41] |
| Cast-T6 GZ15K | Peak-200 °C for 49 h | 121 Hv | 0 | [42] |
| Cast-T6 GZ151K | Peak-200 °C for 44 h | 127 Hv | 0 | [42] |
| Cast-T6 GZ121K | Peak-225 °C for 8 h | 119 Hv | 0 | [43] |
| Cast-T6 GW63K | Peak-212 °C for 56 h | 114 Hv | 46 | [44] |
| Cast-T6 GWZ1432K | Peak-225 °C for 8 h | 127 Hv | 24 | [45] |

reach peak aging and decreases the peak aging hardness value. However, the LDED-T6 VZ232K alloy exhibits excellent age-hardening behavior even at high aging temperatures and extended aging times, as evidenced by the data in Table 4. It is widely acknowledged that variations in hardness among alloys are primarily associated with solid-phase transformations and changes in the morphology of aging-precipitated phases [38]. At an aging temperature of 280 °C, the hardness gradually decreases with prolonged aging time, followed by a sharp decline after 16 h, and no hardness plateau is observed, as shown in Fig. 17. Based on the corresponding morphology of the nano-precipitated phases, it is evident that both the $\beta'$ and $\beta_1$ phases undergo accelerated growth as aging time increases. Specifically, the rhombic $\beta_1$ phase experiences a significant increase in size, from 13 nm to 65 nm, over the aging period from 4 h to 55 h (see Fig. 18b, d, and f). The three-directional cross-interlocked structure is only observed during the peak aging period at 280 °C, with the corresponding hardness reaching 140 Hv. Therefore, it can be inferred that the formation of the three-directional cross-interlocked structure also contributes positively to hardness. As demonstrated by the results of the precipitated phases aged at 220 °C and 250 °C (Figs. 9f, h and Figs. 10d, f), a slight increase in the size of the $\beta'$ phase is observed with extended aging time, while the size of the $\beta_1$ phase remains relatively stable, and the precipitated phases consistently maintain a three-directional cross-interlocked structure. Thus, it can be concluded that two factors contribute to the emergence of the high hardness plateau: first, the higher density and smaller size of the $\beta'$ and $\beta_1$ phases, and second, the persistent presence of precipitated phases with a three-directional interlocking lattice structure.

## 5. Conclusion

(1) The as-deposited VZ232K alloy exhibited fine equiaxed grains (11.9 ± 2.1 μm) and a continuous reticular network of eutectic phases, attributed to the ultra-high Gd content and the high cooling rate of the LDED process. The ultimate tensile strength (UTS), yield strength (YS), and elongation (EL) of the as-deposited LDED VZ232K alloy were 326 ± 4 MPa, 287 ± 3 MPa, and 2.1 ± 0.2%, respectively. The high yield strength of the as-deposited VZ232K alloy was primarily due to grain boundary strengthening. However, crack propagation along the grain boundary eutectic phase resulted in poor plasticity.

(2) Solution heat treatment led to the transformation of the eutectic phase from a continuous reticular network to isolated islands, accompanied by the formation of stacking faults (SFs) with excellent coordinated deformation and fine lamellar LPSO phases within the grains. The fracture mode transitioned from intergranular to transcrystalline fracture, which was associated with the transformation and formation of the second phases. This resulted in a significant increase in elongation to 8.9 ± 0.4%.

(3) The peak-aged LDED-T61 VZ232K alloy demonstrated superior mechanical properties, with a UTS of 424 ± 6 MPa, a YS of 326 ± 4 MPa, and an EL of 3.4 ± 0.2%. The ultra-high number density ($2.4 \times 10^4$ $\mu m^{-2}$) and fine size (6.4 nm × 5.5 nm) of the $\beta'$ phase contributed to exceptional precipitation strengthening. The over-aged specimens exhibited an extended high hardness plateau (above 138 Hv) and maintained high yield strength (above 300 MPa). The formation of the $\beta'$ phase with a three-way interlocking lattice structure enhanced the yield strength and hardness of the alloy.

## Declaration of competing interest

The authors declare that they have no known competing financial interests or personal relationships that could have appeared to influence the work reported in this paper.

## CRediT authorship contribution statement

**Zhe Xu:** Writing – review & editing, Writing – original draft, Visualization, Software, Methodology, Investigation, Formal analysis, Data curation, Conceptualization. **Zhuo Li:** Writing – review & editing, Resources, Project administration, Funding acquisition, Data curation, Conceptualization. **Chunjie Shen:** Writing – review & editing, Validation, Methodology, Formal analysis. **Dongdong Zheng:** Writing – review & editing, Visualization, Supervision, Methodology, Formal analysis, Conceptualization. **Yuxuan Tu:** Writing – review & editing, Validation, Resources, Investigation, Conceptualization.

## Acknowledgment

This work is financially supported by the National Key Research and Development Pragram of China (Grant No. 2023YFB4603300).

## References

[1] X. Zhang, Y. Chen, J. Hu, Progress in Aerospace Sciences 97 (2018) 22–34.
[2] J. Yang, Z. Zhu, S. Han, et al., J Alloys Compd (2024) 1008.
[3] J. Zhang, S. Liu, R. Wu, et al., Journal of Magnesium and Alloys 6 (3) (2018) 277–291.
[4] J.M. Meier, J. Caris, A.A Luo, Journal of Magnesium and Alloys 10 (6) (2022) 1401–1427.
[5] M. Li, G. Zhang, S. Yin, et al., Journal of Magnesium and Alloys 12 (5) (2024) 1867–1879.
[6] Y. Zhang, W. Rong, Y. Wu, et al., J Alloys Compd 777 (2019) 531–543.
[7] E. Sitzmann, E.A Marquis, Philos Mag Lett 95 (1) (2015) 7–13.
[8] L. Yang, H. Shi, Y. Huang, et al., Materials Science and Engineering (2024) 900.
[9] Y. Jiang, H. Tang, Z. Li, et al., Additive Manufacturing (2022) 59.
[10] H.R .J Nodooshan, W. Liu, G. Wu, et al., Materials Science and Engineering 615 (2014) 79–86.
[11] Q. Deng, X. Wang, Q. Lan, et al., Mater Charact (2022) 190.
[12] X. Jiang, S. Hu, L. Wang, Materials Science and Engineering (2023) 883.

[13] D. Deng, R. Cheng, B. Jiang, J Alloys Compd (2023) 968.
[14] G. Wu, X. Tong, C. Wang, et al., Journal of Magnesium and Alloys (2023).
[15] Y. Lin, S. Wu, Y. Wang, et al., Journal of Materials Research and Technology (2025).
[16] Y. Jiang, Q. Le, Y. Zhu, et al., J Alloys Compd (2024) 970.
[17] Q. Deng, F. Chen, L. Wang, et al., Journal of Materials Science & Technology (2024).
[18] E.A. Antillon, C.A. Hareland, P.W Voorhees, Acta Mater (2023) 248.
[19] D. Yin, A. Misra, J Alloys Compd (2023) 966.
[20] Q. Deng, Z. Chang, N. Su, et al., Journal of Magnesium and Alloys (2023).
[21] J. Zhan, G. Wu, X. Tong, et al., Journal of Magnesium and Alloys (2024).
[22] D. Zheng, Z. Li, Y. Jiang, et al., Additive Manufacturing (2022) 57.
[23] Y. Jiang, H. Tang, Z. Li, et al., J Alloys Compd (2024) 1005.
[24] Q. Wu, Y. Wu, Q. Deng, et al., Journal of Magnesium and Alloys (2024).
[25] Q. Cao, C. Zeng, B. Qi, et al., Additive Manufacturing (2023) 67.
[26] X. Gao, B.C. Muddle, J.F Nie, Philos Mag Lett 89 (1) (2009) 33–43.
[27] Q. Deng, Y. Wu, W. Zhu, et al., Materials Science and Engineering (2022) 829.
[28] X. Zhang, Y. Shi, J. Li, et al., Journal of Materials Research and Technology 29 (2024) 1601–1615.
[29] Y. He, R. Guo, X. Zhao, et al., Journal of Rare Earths 42 (12) (2024) 2217–2230.
[30] Z. Deng, Q. Su, M. Chen, et al., Journal of Magnesium and Alloys (2024).
[31] X.I.A.O.L. Wang N, S. Luo, et al., Journal of Materials Research and Technology 27 (2023) 4356–4365.
[32] G. Liu, G.J. Zhang, F. JIANG, et al., Nat Mater 12 (4) (2013) 344–350.
[33] Y.Z. Ji, A. Issa, T.W. Heo, et al., Acta Mater 76 (2014) 259–271.
[34] Q. Deng, Y. Wu, Q. Wu, et al., Additive Manufacturing (2022) 49.
[35] Q. Cao, C. Zeng, X. Cai, et al., Additive Manufacturing (2023) 76.
[36] S. Shen, Y. Zhuang, M. Li, et al., Journal of Magnesium and Alloys 11 (11) (2023) 4263–4273.
[37] C. Shen, Y. Tu, X. Cheng, et al., J Alloys Compd (2024) 986.
[38] H. Cai, Z. Zhao, Q. Wang, et al., Materials Science and Engineering: A (2022) 849.
[39] H. Liao, P. Fu, L. Peng, et al., Materials Science and Engineering: A 687 (2017) 281–287.
[40] P. Bai, J. Wang, Z. Zhao, et al., Journal of Materials Research and Technology 27 (2023) 5805–5821.
[41] T. Ozaki, Y. Kuroki, K. Yamada, et al., Materials Transactions 49 (10) (2008) 2185–2189.
[42] W. Rong, Y. Wu, Y. Zhang, et al., Mater Charact 126 (2017) 1–9.
[43] D. Wang, P. Fu, L. Peng, et al., Mater Charact 153 (2019) 157–168.
[44] Q. Wang, L. Xiao, W. Liu, et al., Materials Science and Engineering 705 (2017) 402–410.
[45] S. Zhang, W. Liu, X. Gu, et al., J Alloys Compd 557 (2013) 91–97.